Journal of Environmental Chemical Engineering 14 (2026) 123900

Contents lists available at ScienceDirect

Journal of Environmental Chemical Engineering

journal homepage: www.elsevier.com/locate/jece

Crawfish shell-based biosorbents for rare earth element (Nd(III)) immobilization in aqueous solution

Balazs Bencsik [a], Jessica Davis [b], Thomas Elder [c], Yucheng Peng [d,*]

[a] College of Forestry, Wildlife, and Environment, Auburn University, 602 Duncan Drive, Auburn, AL 36849, United States
[b] Soil, Forage, & Water Testing Laboratory Auburn University, 961 S Donahue Dr, Auburn, AL 36849, United States
[c] College of Forestry, Wildlife, and Environment, Auburn University, 602 Duncan Drive, Auburn, AL 36849, United States
[d] College of Forestry, Wildlife, and Environment, Auburn University, 602 Duncan Drive, Auburn, AL 36849, United States

ARTICLE INFO

Keywords:
Nd(III)
Rare earth elements
Crawfish shell waste
Biochar
Dissolution-precipitation
Immobilization

ABSTRACT

Pristine crawfish shell waste and shell-derived biochars produced at 500, 650, and 800 °C were evaluated as calcium-rich sustainable biosorbents for Nd(III) immobilization from aqueous solution. Batch experiments were conducted at 23 °C using 50 mL of 1000 mg L^{-1} Nd(III) solution and sorbent mass of 25–100 mg to investigate removal behavior, kinetics, and mechanisms. The 800 °C biochar exhibited the highest apparent Nd(III) removal capacity (1200 mg g^{-1}), which was attributed to instantaneous alkaline precipitation and the formation of Nd $(OH)_3$. In contrast, pristine crawfish shell and the 500 and 650 °C biochars immobilized Nd(III) primarily through a dissolution–precipitation mechanism, yielding amorphous and crystalline Nd-containing carbonate phases. Among these sorbents, pristine crawfish shell showed the highest removal capacity at a sorbent mass of 25 mg (574.8 mg g^{-1}), followed by the 500 °C biochar (490.1 mg g^{-1}), whereas the 650 °C biochar exhibited substantially lower performance (291.4 mg g^{-1}). Except for the 800 °C biochar, for which removal was instantaneous, the Elovich model provided the best fit to the kinetic data across pristine shell, 500 °C, and 650 °C sorbent types, regardless of the sorbent mass. The strong correlation between Ca(II) release and Nd(III) removal, supported by XRD, FTIR, and SEM–EDS analyses, indicates that Nd(III) immobilization is governed by phase-dependent dissolution of calcium carbonate substrates followed by reprecipitation of Nd phases. These findings demonstrate that crawfish shell waste can serve as a highly efficient sacrificial biogenic calcium carbonate precursor for Nd(III) immobilization, even under ambient conditions.

1. Introduction

Rare earth elements (REEs) are indispensable to a wide range of modern technologies and advanced functional materials. Due to the continuously increasing demand for rare earth minerals, attention has expanded beyond primary ore deposits such as bastnäsite, monazite, xenotime, and euxenite [1,2]. Secondary sources, including red mud, phosphate mine tailings, coal mine drainage, coal fly ash, and electronic waste, have attracted significant interest as potential alternative resources [3].

Neodymium (Nd) is one of the most critical rare earth elements (REEs), used extensively in high-performance permanent magnets that are essential for clean-energy and advanced technologies, including electric vehicle motors and wind turbine generators [4]. Industrial-scale rare earth element separation is primarily achieved through solvent extraction, which remains the dominant technology, supported by ion exchange, selective precipitation, and, to a lesser extent, membrane- and adsorption-based techniques [5]. The growing demand for REEs, coupled with limited primary supply and environmentally damaging extraction processes, has spurred research into sustainable recovery and separation methods [6]. Therefore, bio-based sorbents and precipitating agents derived from residual or byproduct materials have gained attention as eco-friendly, low-cost tools for REE immobilization and recovery. In recent decades, several residue-derived biomaterials such as marine algae [7], walnut shells [8], bone powder [9], eggshells [10], [11], and crab shells [12] have been extensively investigated and have demonstrated excellent potential for the recovery of REEs from aqueous solutions. The REE ions in aqueous solutions can be removed via various mechanisms, including surface complexation, electrostatic interactions, ion exchange, physisorption, or precipitation, which represent distinct

* Corresponding author.
E-mail addresses: bab0218@auburn.edu (B. Bencsik), jld0084@auburn.edu (J. Davis), eldertj@auburn.edu (T. Elder), yzp0027@auburn.edu (Y. Peng).

https://doi.org/10.1016/j.jece.2026.123900
Received 14 April 2026; Received in revised form 5 June 2026; Accepted 29 June 2026
Available online 30 June 2026

immobilization pathways [13]. The formation of heavy-metal carbonates through precipitation in the presence of solid-phase inorganic calcite is well documented, and the primary objective in such systems is typically to maximize heavy-metal immobilization from various sources (e.g., acid mine drainage, wastewater) [14–17]. The same principle also applies to Ce(III) and Eu(III) ions in aqueous solution in the presence of calcium-carbonate-rich pristine crab shell, particularly at elevated pH (around pH 6), as reported by Vijayaraghavan and Balasubramanian [12]. In aqueous systems that are at or above calcite saturation, REEs are expected to occur mainly as carbonate complexes, with $REECO_3^+$ and/or $REE(CO_3)_2^-$ dominating depending on the solution pH [18,19].

Rateau et al. [10] investigated the use of eggshell waste as a sustainable sacrificial substrate for the capture of lanthanum, neodymium, and dysprosium from aqueous solution through a dissolution–reprecipitation mechanism at hydrothermal conditions from 30 to 205 °C. Here, dissolution–reprecipitation refers to a coupled mineral transformation in which partial dissolution of the parent calcium carbonate phase creates local supersaturation, followed by precipitation of a new REE-bearing carbonate or hydroxycarbonate phase at or near the reaction interface [20]. However, below 90 °C no REE immobilization occurred even after 14 weeks, while at 90 °C the process only began after 7 days and proceeded with very low efficiency.

Szucs et al. [21] studied La(III), Nd(III), and Dy(III) reaction pathways on calcite at 21 °C and hydrothermal conditions. They reported a prolonged precipitation process, occurring after 14 days in the La experiments but requiring up to 145 days in the Nd and Dy experiments (50 mg calcite, 50 mL of 10 mM rare earth-bearing aqueous solution). In contrast, elevated hydrothermal conditions (50–220 °C) markedly accelerated the mineral replacement of calcite by REE carbonates.

In dissolution–reprecipitation systems, two fundamental objectives are (i) to maximize substrate dissolution and (ii) to obtain the desired carbonate phases with high purity [22]. If the precursor substrate persists after the reaction, the post-processing and separation of the final product would become significantly more complicated [10]. The crystallization of REE carbonates from aqueous media follows a consistent non-classical pathway initiated by metastable amorphous precursor phases, with the transformation process governed by temperature, REE concentration, ionic radii, molar ratios, and the structure and chemistry of the host carbonate [23] [24]. At lower temperatures ($\leq$ 60 °C), the amorphous precursor typically crystallizes into hydrated phases, such as lanthanite [$REE_2(CO_3)_3{\cdot}8\ H_2O$], or tengerite [$REE_2(CO_3)_3{\cdot}2–3H_2O$]. At hydrothermal temperatures (T $\geq$ 95 °C), the system transforms into anhydrous hydroxycarbonates, predominantly the orthorhombic REE-$CO_3(OH)$ phase (kozoite), which ultimately converts to the hexagonal polymorph $REECO_3(OH)$ (hydroxylbastnäsite) [25–28]. Interface-coupled dissolution and precipitation take place whenever thermodynamic disequilibrium exists between a fluid and a solid [29]. However, the complete dissolution of the substrate during a dissolution–reprecipitation reaction can be inhibited when a water-tight crust of the newly precipitated phase forms around the remaining core (template effect). Once partial equilibrium is established within this isolated fluid layer, further dissolution ceases, and recrystallization terminates [30].

In contrast to dissolution–reprecipitation mechanisms, in which calcium carbonate acts as a sacrificial precursor, calcium carbonate can also function as a sorbent for immobilizing REE ions from aqueous solutions at near-neutral to alkaline pH (typically pH 7–9). While dissolution–reprecipitation reactions can be strongly accelerated by hydrothermal conditions [21,31], surface sorption processes are primarily governed by the solution pH, which controls the speciation of REE ions and their mode of interaction with the calcium carbonate surface [32]. Under near-neutral to alkaline pH conditions, lanthanoid ions adsorb onto the calcite surface predominantly as mono- and di-hydroxo complexes rather than forming discrete REE-carbonate precipitates [33,34].

While some studies have investigated the ability of calcined crustacean shells to remove various inorganic and organic aqueous contaminants, such as heavy metal ions, and phosphate from aqueous solutions [35,36], no study to date has specifically examined the effectiveness of pristine and calcined crawfish shell in immobilizing REEs from REE-bearing solutions. Therefore, crawfish shell was selected because it is a naturally occurring organic–inorganic composite mainly composed of calcium carbonate, chitin, and proteins. Among these components, the biomineral calcium carbonate fraction is particularly important because it can act as a reactive carbonate source and directly contribute to precipitation-based REE removal. This concept is supported by previous work on crab shell particles, a closely related crustacean shell material, where calcium carbonate was identified as the main component responsible for Ce(III) and Eu(III) removal through carbonate-mediated microprecipitation on the shell surface [12]. Therefore, this study investigates the Nd(III) removal capacity of pristine crawfish shell and shell-derived biochars produced at different pyrolysis temperatures (500, 650, and 800 °C) under ambient conditions, without the need for hydrothermal treatment. Nd(III) was selected as a representative trivalent REE ion to evaluate crawfish shell-derived sorbents as sacrificial carbonate-containing sorbent for REE immobilization, rather than as exclusively Nd(III)-specific sorbents. Beyond evaluating removal performance, the study aims, for the first time to elucidate the underlying removal mechanisms, crystallization pathways, structural features, and elemental distribution of the reaction products formed during interactions between high concentration Nd(III) aqueous solution and the shell-derived sorbents.

2. Materials and methods

2.1. Preparation of biochar

Crawfish, also known as crayfish, were purchased from a local market in Auburn, Alabama, USA. The crawfish were boiled, and the shells were separated, then thoroughly rinsed several times with deionized (DI) water to remove residual impurities such as remaining tissue and salt. The cleaned shells were oven-dried at 105 °C for 6 h and subsequently crushed to particle sizes in the range of 1–2 mm.

The dried shells were then placed in a quartz tube furnace (GSL−1100X, MTI Corporation, Richmond, CA, USA) under a nitrogen atmosphere. Pyrolysis was performed at 500, 650, and 800 °C, and the resulting biochar sorbents were denoted as 500, 650, and 800, respectively. Untreated pristine crawfish shell was also used in the removal experiments as a reference and was denoted as PCS. The temperature program for biochar production consisted of four steps: (1) heating from room temperature at a rate of 10 °C min^{-1} , (2) holding at the target temperature for 1 h, (3) cooling at 10 °C min^{-1} to 200 °C, and (4) natural cooling from 200 °C to room temperature. Once the biochar samples reached room temperature, they were ground using a mortar and pestle and then sieved through a 200-mesh (75 μm) sieve. Particles that passed the 200-mesh sieve were collected and used for subsequent analyses.

2.2. Experimental procedure for Nd(III) removal and immobilization

Neodymium chloride, anhydrous (Thermo Scientific Chemicals, purity: 99.9%, residual water: $\leq$1.0%) was dissolved in deionized water to prepare a 1000 mg L^{-1} Nd(III) stock solution. Removal kinetics experiments were conducted in 50 mL polypropylene centrifuge tubes using sorbent masses of 25, 50, 75, and 100 mg. The suspensions were mixed on a tube rotator (Scilogex Sci-RL-E, Rocky Hill, CT, USA) at 40 rpm and 23 °C for 72 h. At predetermined time points (0.5, 2, 4, 8, 12, 24, 48, and 72 h), samples were collected from the tubes using syringes, and the liquid phase was separated by filtration through a 0.45 μm PTFE membrane to remove suspended solids prior to analysis. The residual Nd (III) concentration and the released Ca(II) concentration in the filtrate were determined using ICP-OES (Agilent 5800, Santa Clara, CA, USA). The emission signal of Nd(III) was measured at 401.224 nm, while that

of Ca(II) was measured at 317.933 nm. After 72 h, the remaining biochar was recovered by vacuum filtration using a 0.45 μm nylon membrane filter and dried at 90 °C for 2 h. The pH of the Nd(III)–sorbent suspension was not adjusted by adding acid or base. All experiments were performed in triplicate. The removal capacity at time t (q_t) and the removal efficiency (R, %) were calculated using the following equations:

$$q_t = \frac{(C_0 - C_t) \times V}{m} \quad (1)$$

$$R \quad (\%) = \frac{(C_0 - C_t)}{C_0} \times 100 \quad (2)$$

where q_t and R are removal capacity (mg g^{-1}) and removal rate (%) at time t (h), respectively; C_0 and C_t represent the initial concentrations of Nd(III) and the Nd(III) concentration at time t (mg L^{-1}) respectively. V is the solution volume (L) and m is the mass of sorbent (g).

The amount of Ca(II) released into solution at time t, expressed as Ca (II) release ($q_{Ca,t}$), was calculated using Equation (3):

$$q_{Ca,t} = \frac{C_{Ca,t} \times V}{m} \quad (3)$$

where $q_{Ca,t}$ is the Ca(II) release at time t (mg g^{-1}), $C_{Ca,t}$ is the dissolved Ca(II) concentration at time t (mg L^{-1}), V is the solution volume (L) and m is the mass of sorbent (g).

The fraction of total Ca released into solution as Ca(II) was calculated using Equation (4):

$$F_{Ca,t} = \frac{q_{Ca,t}}{C_{Ca,total}} \times 100 \quad (4)$$

where $F_{Ca,t}$ is the fraction of total Ca released into solution as Ca(II) (%), $q_{Ca,t}$ is the amount of Ca(II) released at time t (mg g^{-1}) and $C_{Ca,total}$ is the total Ca content of the sorbent determined by acid leaching (mg g^{-1}).

2.3. Acid leaching for acid-soluble Ca determination

Acid leaching was performed to quantify the acid-soluble Ca content of the original sorbents. Briefly, 50 mg of each sorbent was treated with 30 mL of 0.2 N HCl for 12 h under continuous mixing. After leaching, the suspension was filtered through a 0.45 μm membrane, and the leachate was analyzed by ICP-OES (Agilent 5800, Santa Clara, CA, USA) to determine the dissolved Ca concentration. The measured Ca concentration was then used to calculate the acid-soluble Ca content of each sorbent. All measurements were performed in triplicate.

2.4. Kinetic modelling

The Nd(III) removal kinetics were evaluated using the pseudo-first order (PFO), pseudo-second order (PSO), and Elovich models to assess potential non-equilibrium behavior. The PFO model is commonly associated with diffusion-related uptake, whereas the PSO model is often used to describe processes dominated by interactions at the solid–liquid interface. The Elovich model is frequently applied to systems exhibiting chemisorption behavior [37]. The PFO, PSO, and Elovich models are given by Equations (5), (6), and (7), respectively [38].

$$q_t = q_e(1 - e^{-k_1 t}) \quad (5)$$

$$q_t = \frac{k_2 q_c^2 t}{1 + k_2 q_e t} \quad (6)$$

$$q_t = \frac{1}{b}\ln(abt) = \frac{1}{b}\ln(ab) + \frac{1}{b}\ln(t) \quad (7)$$

where q_e is the removal capacity (mg·g^{-1}), k_1 (min^{-1}) and k_2 (mg·g^{-1} min^{-1}) are the rate constants for PFO and PSO processes, respectively, α is the initial sorption rate (mg·g^{-1} min^{-1}), while β is the desorption constant (g·mg^{-1}). Regression analyses of the kinetic models were performed using OriginPro software (OriginLab Corporation, Northampton, MA, USA).

Following the approach proposed by Wu et al. [39], the longest contact time in the sorption experiments was selected as the reference time t_{ref}, and the corresponding removal capacity (reference removal capacity) was defined as $q_{ref} = q(t)$. Therefore, Equation (7) can be rewritten as:

$$q_{ref} = \frac{1}{b}\ln(abt) = \frac{1}{b}\ln(ab) + \frac{1}{b}\ln(t_{ref}) \quad (8)$$

2.5. Characterization methods

The pH of the pristine crawfish shell (PCS) and biochar samples (500, 650, and 800) was determined by adding 100 mg of sample to 10 mL of deionized water in 50 mL centrifuge tubes. The suspensions were then mixed using a Scilogex Sci-RL-E tube rotator (Rocky Hill, CT, USA) at a rotation speed of 20 rpm for 1 h, followed by a standing period of 30 min. The pH of the biochar samples was measured using an Extech EC600 pH and digital conductivity meter (Waltham, MA, USA). The pH of the Nd(III)–sorbent suspension during the kinetic experiments was also determined.

The pristine crawfish shell was powdered, homogenized, and passed through a 75 μm (200 mesh) sieve prior to thermogravimetric analysis (TGA) to examine the thermal decomposition of the shell components during pyrolysis. The analyses of the pristine crawfish shell were performed using a TA Instruments TGA Q50 thermogravimetric analyzer. The samples were heated from 23 to 900 °C at a heating rate of 10 °C/min under a nitrogen atmosphere.

Fourier transform infrared spectroscopy (FT-IR) was used to characterize the surface functional groups of the samples before and after the kinetic experiments in the wavenumber range of 650–4000 cm^{-1} using a PerkinElmer Spectrum Two FT-IR spectrometer (Waltham, MA, USA) equipped with an attenuated total reflectance (ATR) accessory.

A Rigaku SmartLab powder X-ray diffractometer (Rigaku Corporation, Tokyo, Japan) was used to analyze the phase composition of all samples using Cu Kα radiation at 40 kV and 30 mA, over a 2θ range of 10°–80°, with a step size of 0.01° and a scan rate of 1.5 min per degree. Phase identification was performed by comparison with the literature and with reference patterns from the publicly available database using Profex 5.6.1 software (Profex Doebelin, Solothurn, Switzerland).

SEM–EDS analyses were conducted to evaluate morphological changes and surface elemental composition of the sorbents before and after Nd(III) sorption using a ZEISS EVO 10 scanning electron microscope (Carl Zeiss AG, Germany) equipped with an EDAX TEAM Element EDS system (USA). The samples were gold-coated for SEM imaging, while uncoated samples were used for EDS analysis to avoid interference from the strong gold signal. The images were acquired at an accelerating voltage of 20 keV using a secondary electron detector with an objective aperture of 30 μm.

3. Results and discussion

3.1. Characterization of pristine crawfish shell and biochars prepared at different pyrolysis temperatures

According to Chen et al. [40], crawfish shells typically consist of protein (20–30%), calcium carbonate (30–40%), and chitin (20–30%) on a dry-weight basis. The corresponding decomposition temperatures of these components can be observed in the weight–temperature (TG) and derivative weight–temperature (DTG) curves (Supplementary Fig. S1). The thermal decomposition behavior of the crawfish shell showed good agreement with the results reported by Romano et al. [41] for lobster shell. The decomposition of the protein fraction was largely completed at approximately 270 °C, after which chitin decomposition

became dominant. Based on the DTG curve, the maximum decomposition rate of chitin was observed at 297 °C. Chitin degradation then continued over a broad temperature range, with substantial mass loss up to around 370 °C and nearly complete degradation between 300 and 600 °C. This behavior is consistent with lobster shell results reported by Alonso et al. [42]

The DTG maximum at 661 °C coincides with the main mass-loss step observed between 600 and 750 °C, suggesting thermal destabilization and transformation of the metastable vaterite (a metastable crystalline phase of calcium carbonate) fraction. This mass-loss event may reflect carbonate-phase rearrangement and partial CO_2 release rather than complete decarbonation.

Fig. 1 shows the X-ray diffraction patterns of the four examined sorbent materials. Depending on the applied pyrolysis temperature, different crystalline phases can be observed. In the XRD pattern of (PCS) (Fig. 1a), a broad crystalline reflection around 19° (2θ) is observed, which diminishes after pyrolysis.

This reflection is commonly associated with chitin [43], which diminishes upon pyrolysis [44,45]. Calcite peaks (JCPDS card No. 05–0586) were identified in the XRD patterns of the PCS (Fig. 1a) and 500 (Fig. 1b) and 650 (Fig. 1c). In addition to calcite, vaterite peaks (JCPDS card No. 72–0506) were also detected in PCS (Fig. 1a) and 500 (Fig. 1b). The organic matrix is considered to play a principal role in biomineralization processes by influencing the formation of calcium carbonate polymorphs, mainly calcite, with minor amounts of aragonite (an orthorhombic $CaCO_3$ polymorph), and vaterite [46]. Vaterite is the least thermodynamically stable anhydrous calcium carbonate polymorph, and its occurrence is relatively rare in nature [47,48]. However, it has been reported in eggshells from birds [49], in freshwater cultured pearls and mussel shells [50,51], gallstones [52] and crawfish shells [53]. Since the metastable vaterite phase was not detected after pyrolysis at 650 °C, and no CaO or $Ca(OH)_2$ phases were observed in 650, the DTG peak at 661 °C likely reflects thermal rearrangement of Ca-carbonate phases rather than decarbonation.

In the 800 sample, the calcite peaks disappeared due to the decarbonation of calcium carbonate, while peaks corresponding to calcium hydroxide ($Ca(OH)_2$) (portlandite, JCPDS card No. 04–0733) and calcium oxide (CaO) (lime, JCPDS card No. 37–1497) appeared (Fig. 1d).

Fig. 2 shows the FTIR spectra of the four examined sorbent materials. The FTIR spectra of the pristine and biochar samples show characteristic bands of carbonate groups associated with calcium carbonate phases.

In all of the spectra, the band at 1044 cm^{-1} is attributed to the ν_1 symmetric stretching vibration of the CO_3^{2-} group. The characteristic ν_2 out-of-plane deformation band, common to both calcite and vaterite,

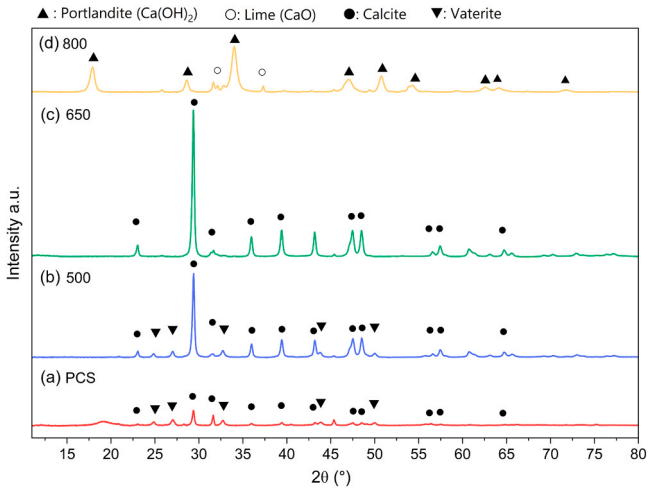

Fig. 1. X-ray diffraction patterns of different sorbents before the sorption experiment.

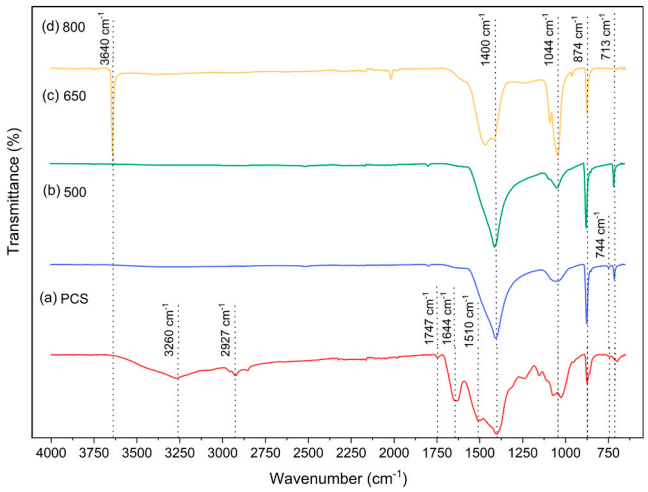

Fig. 2. FTIR spectra of different sorbents before the sorption experiment.

appears at 874 cm^{-1} . The band around 1400 cm^{-1} corresponds to the ν_3 asymmetric stretching vibration of the carbonate group. For PCS (Fig. 2a), the ν_4 in-plane bending vibration of polyphase calcite is observed at 700 cm^{-1} , whereas for 500 (Fig. 2b) and 650 (Fig. 2c) the same vibration occurs at 713 cm^{-1} . The characteristic ν_4 band of polyphase vaterite at 744 cm^{-1} was not detected in the spectra of 650 (Fig. 2c) and 800 (Fig. 2d). The bands at 700 cm^{-1} , 713 cm^{-1} and 744 cm^{-1} are consistent with those reported for calcite and vaterite calcium carbonate phases [54,55]. Although crystalline $CaCO_3$ phases were no longer detected by XRD after pyrolysis at 800 °C, the carbonate-related bands observed by FTIR indicate the presence of surface or amorphous carbonate species.

In PCS (Fig. 2a), a broad band centered around 3260 cm^{-1} can be observed, which is attributed to overlapping O–H and N–H stretching vibrations associated with hydroxyl groups, adsorbed water, and amide functionalities of chitin and proteins. Distinct bands are also observed at approximately 2927–2929 cm^{-1} which is assigned to the asymmetric and symmetric stretching vibrations of aliphatic –CH_2– groups [56]. In addition, two carbonyl-related bands can be observed in the FTIR spectrum of PCS (Fig. 2a) a weak band at 1747 cm^{-1} , assigned to the C═O stretching vibration of esterified or acetyl-type carbonyl groups associated with polysaccharide structures. A more pronounced band at 1644 cm^{-1} corresponds to the amide I vibration (C═O stretching), while a band around 1510 cm^{-1} is associated with amide II vibrations of chitin and/or residual proteins [56,57]. This band progressively weakened with increasing pyrolysis temperature and was substantially reduced or absent in the biochar samples, indicating the thermal degradation of polysaccharide-associated oxygen-containing functional groups [58].

In contrast, the FTIR spectrum of the 800 sample (Fig. 2d) shows a narrow band close to 3640 cm^{-1} , which is assigned to $Ca(OH)_2$ formed after high-temperature treatment. This band corresponds to the stretching vibration of hydroxyl groups associated with hydroxide species [59]. This was also confirmed by X-ray diffraction results.

With increasing pyrolyzing temperature, the pH of the samples increased progressively, from the lowest value observed from the PCS (pH 9.28) to 500 (pH 10.26), 650 (pH 12.18), and 800 (pH 12.58). The pH of the aqueous suspension of the calcium-rich sorbent is primarily governed by the dissolution of carbonate phases and the hydration of oxide-derived species, which release carbonate species and hydroxide ions into the solution. During this process, Ca(II) released from the crawfish shell–derived material participates in carbonate equilibria and hydroxide formation (e.g., $CaCO_3$ and $Ca(OH)_2$), resulting in a strongly alkaline aqueous environment.

To further quantify the amount of acid-soluble Ca-bearing phases in the original sorbents, acid leaching was performed, and the results are

summarized in Table 1. The released Ca(II) content was expressed as mg g^{-1} of sorbent.

For PCS, 500, and 650, the measured Ca(II) content was also converted to $CaCO_3$-equivalent content, because XRD and FTIR results indicated that the Ca-containing crystalline phases in these sorbents were mainly associated with calcium carbonate phases. The conversion was based on the acid dissolution reaction:

$$CaCO_3 + 2H^+ \rightarrow Ca^{2+} + CO_2 + H_2O$$

Based on this calculation, the $CaCO_3$-equivalent content of PCS was 45.1 wt%, which is in good agreement with previously reported calcium carbonate contents for crawfish shells [40]. The $CaCO_3$-equivalent content increased progressively after thermal treatment, reaching 79.3 wt% for 500 and 85.7 wt% for 650. This enrichment can be attributed to the thermal degradation and carbonization of the protein and chitin matrix, which increased the relative proportion of Ca-bearing inorganic phases in the biochars. For the 800 °C biochar, the $CaCO_3$-equivalent value was not calculated because XRD and FTIR confirmed the presence of mixed CaO and $Ca(OH)_2$ phases, making it impossible to assign the acid-leachable Ca to a single Ca-containing phase. However, this sorbent released a noticeably higher Ca(II) amount of 512.2 mg g^{-1}

3.2. Nd(III) removal kinetics

The removal kinetics of Nd(III) were investigated for four different sorbents at various sorbent masses. While many studies vary the initial metal ion concentration, adjusting the sorbent mass at a fixed solution volume is more relevant for practical applications. In calcium carbonate-based systems, the sorbent mass governs Ca(II) release and carbonate availability, which directly influence supersaturation and the formation of Nd-containing solid phases. These processes also affect the solution pH; therefore, the pH was not externally controlled but allowed to evolve naturally, and was continuously monitored to better understand the underlying mechanisms. Upon contact with the sorbent, the solution pH was self-adjusted depending on the type and amount of sorbent added. Supplementary Figs. S2-S5. shows the pH as a function of time for the four different sorbents and applied sorbent mass. The pH profiles show that PCS, 500, and 650 sorbents maintained near-neutral conditions, with mean pH values ranging from 5.61 to 6.45 across all sorbent masses and contact times. This narrow range indicates only minor fluctuations without any systematic shift in pH during the removal process. In contrast, the biochar produced at 800 °C induced a strong and mass-dependent increase in pH, reaching highly alkaline conditions (pH > 12) at higher masses. This pronounced alkalinity originates from the presence of CaO and $Ca(OH)_2$ phases in the 800 sample.

Fig. 3 shows the Nd(III) removal capacity (mg g^{-1}) as a function of time at a sorbent mass of 25 mg for PCS, 500, 650, and 800. The kinetic fitting results obtained at different sorbent masses are presented in Figs. S6-S8, and the corresponding kinetic parameters are summarized in Tables S1-S3. The PFO, PSO, and Elovich models were applied to identify the most suitable kinetic model for Nd(III) removal. During the first 4 h, PCS and the 500 sample exhibited comparable Nd(III) removal capacity. However, beyond 4 h, PCS showed faster removal kinetics, resulting in higher removal capacity over time. In contrast, 650

Table 1
Acid-leachable Ca content and calculated $CaCO_3$-equivalent content of the sorbents.

Sorbent	Avg. Ca(II) released (mg g^{-1})	SD (mg g^{-1})	Avg. $CaCO_3$equivalent (mg g^{-1})	Avg. $CaCO_3$-equivalent (wt %)
PCS	180.5	2.3	451	45.1
500	317.6	8.6	793	79.3
650	343.3	9.7	857	85.7
800	512.2	12.6	not calculated	not calculated

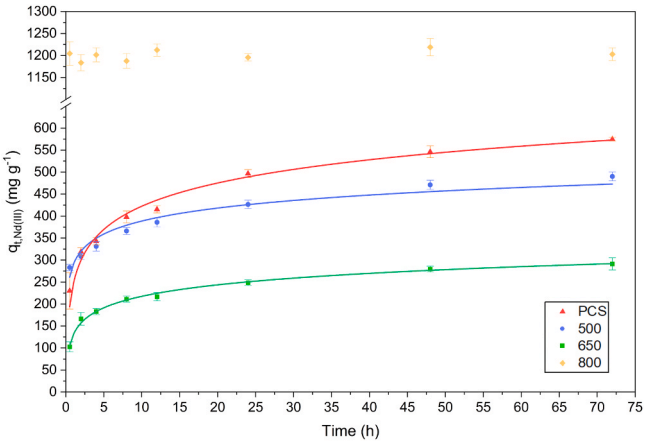

Fig. 3. Nd(III) removal kinetics at a sorbent mass of 25 mg for different sorbents at 23 °C. Elovich model fits are shown for PCS, 500, and 650. Error bars represent the standard deviation.

exhibited a markedly slower removal response throughout the entire experimental period. The 800 showed immediate Nd(III) immobilization due to its strong alkalinity. At the lowest sorbent mass of 25 mg, the apparent removal capacity remained nearly constant over time, with a mean value of 1200.0 mg g^{-1} . At higher sorbent masses, Nd(III) was completely removed from the solution within 30 min, and was no longer detected in the solution. Since the removal was controlled by chemical precipitation rather than sorption kinetics, kinetic model fitting was not performed for this sorbent.

For PCS, 500 and 650, the applied sorbent mass had a pronounced effect on removal behavior. Lower sorbent mass consistently exhibited higher apparent removal capacities, which decreased with increasing sorbent mass. After shaking for 72 h at 23 °C, PCS exhibited the highest Nd(III) removal capacity (574.8 mg g^{-1}), followed by the 500 sample (490.1 mg g^{-1}), whereas the 650 sample showed substantially lower performance (291.4 mg g^{-1}) at a sorbent mass of 25 mg.

Based on visual inspection of the fitting curves (Fig. S6-S8) and the R^2, χ^2, and mean absolute percentage error (MAPE) values (Tables S1-S3), the Elovich model provided a substantially better fit to the kinetic data compared with the PFO and PSO models. The Elovich model yielded R^2 values of 0.942–0.992, χ^2 values of 2.62–31.18, and MAPE values of 1.34–5.42%. The model assumes that the activation energy for sorption increases with sorption time and that the surface of the sorbent is heterogeneous. Although the Elovich model is empirical and does not provide a strict physical interpretation of all parameters, it is widely used to describe chemisorption processes at the sorbate-sorbent interface [60].

In comparison, the PFO model showed poor fitting performance, with R^2 values ranging from 0.297 to 0.683, χ^2 values from 152.91 to 616.88, and MAPE values from 13.16% to 18.56%. The calculated PFO q_e values ranged from 226.3 to 479.5 mg g^{-1} , while the k_1 values ranged from 0.284 to 2.288 h^{-1} . The PSO model provided a moderate improvement over the PFO model, with R^2 values of 0.576–0.859, χ^2 values of 44.48–260.69, and MAPE values of 8.23–12.94%. The calculated PSO q_e values ranged from 239.5 to 520.0 mg g^{-1} , and the k_2 values ranged from 0.0015 to 0.0055.

Although the PSO model improved the fitting quality compared with the PFO model, it remained less accurate than the Elovich model. The PFO model exhibited poor agreement with the experimental data, and no consistent improvement was observed with increasing pyrolysis temperature or sorbent mass. In contrast, the PSO model generally provided better fits than the PFO model, suggesting that the removal process was not governed by simple first-order concentration-dependent uptake. However, the better overall performance of the Elovich model indicates that Nd(III) removal was more likely controlled by

heterogeneous, time-dependent surface reactions and coupled dissolution-precipitation processes rather than simple first- or second-order adsorption kinetics. The modelled results also indicate a continuous, monotonic increase in Nd(III) removal over time, without a clearly defined equilibrium plateau within the investigated time frame. This suggests that the removal process may proceed further with extended contact time.

Direct comparison with literature data is complicated by differences in experimental conditions. Nevertheless, the highest Nd(III) removal capacity among the carbonate-rich sorbents, including PCS, 500 and 650 sorbent types, was 574.8 mg g^{-1} for PCS. This value exceeds most reported values, including those for high-performance sorbents such as carboxylic acid-functionalized porous aromatic frameworks (288.4 mg g^{-1}) [61], magnetic nano-hydroxyapatite (300 mg g^{-1}) [62], and phosphorus-functionalized nanoporous carbon (335.5 mg g^{-1}) [63]. The 800 reached a higher apparent removal capacity with an average of 1200.0 mg g^{-1} , but this value is discussed separately because Nd(III) removal was dominated by rapid alkaline precipitation rather than sorption.

3.3. Ca(II) release and its relationship with Nd(III) immobilization

A previous study investigating the role of $CaCO_3$ in crab shell reported that $CaCO_3$ was mainly responsible for the biosorption of Ce(III) and Eu(III), compared with protein and chitin [12]. To clarify the role of Ca-bearing phases in Nd(III) immobilization, the dissolved Ca(II) concentration was measured together with the Nd(III) concentration during the kinetic experiments. Fig. 4 shows the Ca(II) release profiles obtained at a sorbent mass of 25 mg during the Nd(III) removal experiments.

The corresponding Ca(II) release profiles for higher sorbent masses, including 50, 75, and 100 mg, are provided in Figs. S9-S11. The extent of Ca(II) release depended strongly on the sorbent type and sorbent mass. This behavior is closely related to the mineralogical composition of the sorbents, since calcium carbonate phases, including amorphous calcium carbonate, vaterite, and calcite, have markedly different solubilities [31, 64].

The 800 sorbent showed a rapid Ca(II) release, which remained nearly constant during the sorption kinetics. This rapid release can be attributed to the presence of highly soluble CaO and $Ca(OH)_2$ phases, and it also correlates with the rapid immobilization of Nd(III). In contrast, the calcium-carbonate-rich sorbents showed a monotonic increase in Ca(II) release with contact time. PCS exhibited the highest Ca(II) release, followed by the 500 sorbent, which showed slightly lower Ca(II) release, whereas the 650 sorbent exhibited a substantially lower rate.

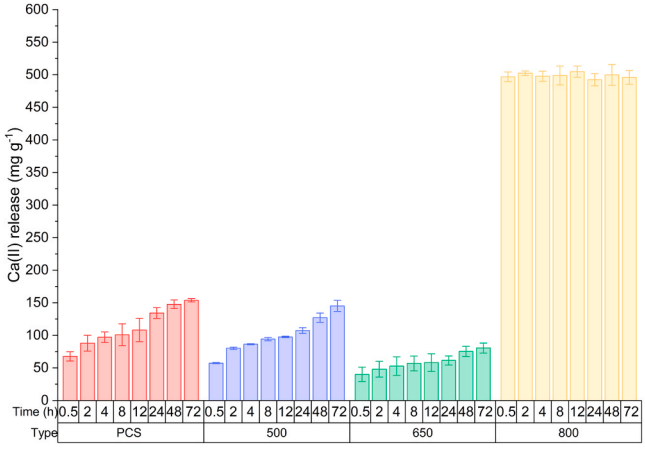

Fig. 4. Time-dependent Ca(II) release from PCS, 500, 650, and 800 sorbents during the Nd(III) sorption experiment using a sorbent mass of 25 mg. Values represent mean ± standard deviation (n = 3).

The highest Ca(II) release from PCS can be partly attributed to the presence of the more soluble amorphous calcium carbonate and vaterite phases, as confirmed by XRD and FTIR analysis. The vaterite phase was also detected in the 500 sorbent, but it was not found in the 650 sorbent. The significant contribution of vaterite to enhanced metal removal, attributed to chemisorption on porous calcite and vaterite particles, was also reported by Sasamoto et al. [65]

Fig. 5 shows the fraction of total Ca released into the solution over the entire sorption period using a sorbent mass of 25 mg, expressed as a percentage of the total Ca content of each sorbent determined by acid leaching (Table 1). This fraction was calculated using Equation (4).

After 72 h of the sorption experiment, 800 showed the highest fraction of total Ca released, reaching 98.9%, followed by PCS at 86.7% and 500 at 48.4%. The 650 sorbent showed the lowest fraction value, with only 25.7% of its total Ca released. Although PCS had the lowest $CaCO_3$-equivalent content among the carbonate-rich sorbents, it released a substantially higher fraction of its total Ca content as Ca(II) compared with the 500 and 650 sorbents. This suggests that, for the calcium carbonate-rich sorbents, a higher $CaCO_3$-equivalent content did not necessarily result in a higher fraction of Ca released into solution. These results further support that the solubility and accessibility of the Ca-bearing phases play a pivotal role in controlling Ca(II) release and, consequently, the immobilization of Nd(III).

Fig. 6 shows the relationship between Ca(II) release and Nd(III) removal capacity using the full dataset for the carbonate-rich sorbents PCS, 500, and 650. The relationship was evaluated to determine whether Ca-bearing phase dissolution was directly linked to Nd(III) immobilization. The sorbent mass-separated plots are provided in Fig. S12 alongside corresponding regression parameters summarized in Table S4.

The consistently high R^2 values (R^2 = 0.89–0.98) obtained for the different sorbent types and sorbent masses show a strong relationship between Ca(II) release and Nd(III) immobilization. Even when all data for the PCS, 500 and 650 sorbents are plotted in Fig. 6, the R^2 value is 0.96 with a narrow confidence interval. In addition, only a few outlier data points can be observed outside the prediction band. This suggests that Ca-containing phases are mainly responsible for the Nd(III) immobilization.

The solid products formed during this process are further examined by XRD, FTIR, and SEM-EDS in the following sections.

3.4. XRD analysis of post-sorption solids

After the 72-hour sorption experiment, the residual solids were filtered, dried, and subsequently characterized by XRD, FTIR, and SEM-EDS to determine the removal mechanisms and the formed neodymium

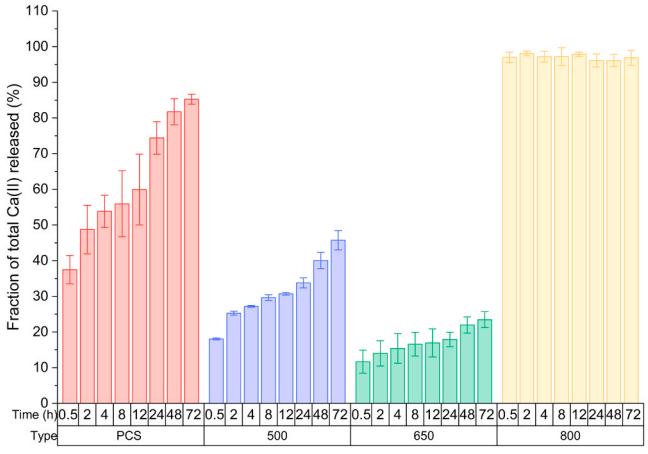

Fig. 5. Fraction of total Ca released as Ca(II) from PCS, 500, 650, and 800 sorbents during the Nd(III) sorption experiment using a sorbent mass of 25 mg.

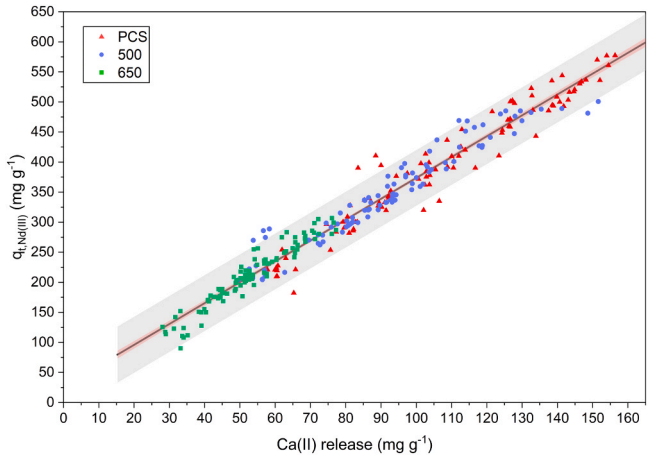

Fig. 6. Correlation between Ca(II) release and Nd(III) removal capacity for PCS, 500, and 650 sorbents using the full dataset obtained with 25, 50, 75, and 100 mg sorbent masses. The solid line represents the linear regression fit, while the shaded area indicates the 95% confidence interval and prediction band.

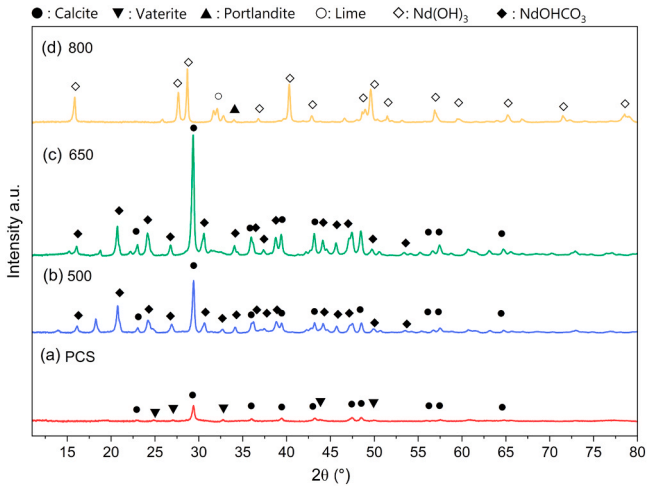

Fig. 7. X-ray diffraction patterns of the different sorbents after 72 h of sorption using a sorbent mass of 25 mg.

phases. Fig. 7 shows the XRD patterns of the four sorbents after the sorption experiments at a sorbent mass of 25 mg. Additional diffraction patterns obtained at different sorbent masses are provided in Supplementary Figs. S13-S16.

In general, the applied sorbent mass did not affect the crystalline phases formed, regardless of sorbent type. However, all sorbents showed clear changes in their XRD patterns after the sorption experiment.

For the 800 sorbent, the presence of CaO and $Ca(OH)_2$ increased the solution alkalinity, leading to the formation of neodymium hydroxide. The characteristic reflections matched hexagonal neodymium hydroxide ($Nd(OH)_3$) (JCPDS card No. 70–0214). [66] The CaO and $Ca(OH)_2$ phases were likely consumed through reaction with the aqueous solution. At sorbent masses of 50, 75, and 100 mg, new calcite reflections emerged at $2\theta = 29.4°$, as shown in Supplementary Figs. S16c-e. The emergence of calcite reflections can be attributed to the partial carbonation of CaO and $Ca(OH)_2$ phases, as well as the presence of carbonate species in the system, as confirmed by FTIR analysis. Limited CO_2 uptake from brief exposure to the atmosphere may have further contributed to calcite formation, as increased CO_2 partial pressure is known to accelerate carbonation [67,68]. Although Nd(III) removal was highly effective, the formation of calcite as a secondary phase is undesirable because it indicates that part of the reactive lime and portlandite was consumed by carbonation rather than exclusively contributing to Nd(III) precipitation. In addition, this phase is detrimental to the purity of the Nd precipitate system. Nevertheless, the almost complete disappearance of lime and portlandite demonstrates that these phases acted as transient alkalinity sources, driving rapid Nd(III) precipitation predominantly as $Nd(OH)_3$.

The XRD patterns obtained after the sorption experiments for both 500 and 650 are in good agreement with literature-reported reflections of neodymium hydroxycarbonate (JCPDS card No. 70–2054) [69]. Notably, the vaterite phase originally present in the 500 °C sample disappeared completely, indicating its complete dissolution during Nd (III) removal. In contrast, reflections corresponding to calcite were still observed at both 500 and 650, suggesting that the calcite phase was not completely consumed. A similar calcite dissolution-precipitation pathway was reported for hen eggshell subjected to hydrothermal treatment by Rateau et al. [10] However, unlike in hen eggshell-based systems, calcium carbonate dissolution in the present system occurred at ambient temperature and did not require hydrothermal treatment.

The X-ray diffraction pattern of PCS after the sorption experiment shows noticeable changes in the peak intensities of both calcite and vaterite. With decreasing sorbent mass, the intensities of the calcium carbonate phases decrease gradually, indicating partial dissolution (Fig. S13). In addition, the characteristic chitin-related peak at 19° (2θ) is also reduced. In contrast to the biochar samples, no crystalline neodymium-containing phase is observed for the PCS after Nd(III) exposure. Similar behavior has been reported in previous studies, where dissolved organic ligands inhibited metal-ion crystallization in aqueous environments, leading to the stabilization of poorly crystalline or amorphous phases [70–72]. The absence of Nd-related crystalline phases in the XRD pattern, together with the partial dissolution of calcium carbonate phases, suggests that Nd(III) may be associated with poorly crystalline or amorphous phases due to the effect of chitin in pristine crawfish shell.

3.5. FTIR analysis of post-sorption solids

Fig. 8 shows the FTIR spectra of the four sorbents after the sorption experiments at a sorbent mass of 25 mg. FTIR spectra obtained at different sorbent masses are presented in Supplementary Fig. S17-S20. In general, varying the sorbent mass did not affect the FTIR spectra of PCS, 500, and 650. However, changes in band intensities and positions were observed for 800. As shown in Fig. 8d and Fig. S20, the slight shift and reduction in intensity of the O-H band from 3643 to 3609 cm^{-1} suggests modification of the Ca-OH environment during

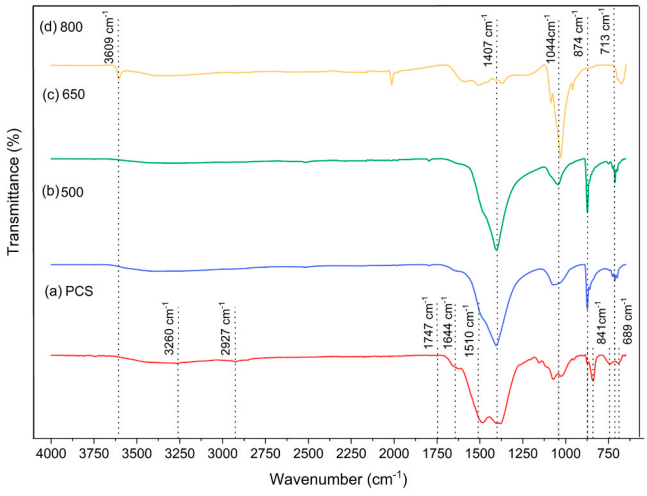

Fig. 8. FTIR spectra of the different sorbents after 72 h of sorption using a sorbent mass of 25 mg.

carbonation rather than the persistence of crystalline $Ca(OH)_2$. Before sorption, a band at 874 cm^{-1} was observed, however, it was not detected after sorption at 25 mg. As the sorbent mass increased to 50 mg and above, this band became more pronounced. Additionally, no band was observed around 700 cm^{-1} before sorption, whereas after sorption, a small band appeared, indicating the formation of a newly precipitated calcite phase in the 800 sample.

Carbonate vibrations dominate the FTIR spectra of 500 and 650 after reaction, with characteristic bands at 1407, 1044, and 874 cm^{-1} . The dominant ν_4 band at 713 cm^{-1} indicates a strong calcite contribution, which may overlap with and obscure bands reported for pure neodymium hydroxycarbonate in the literature [73,74]. In agreement with the XRD results, which show the absence of vaterite-related peaks, the vaterite-associated bending band at 744 cm^{-1} was not detected in the 500 sample.

The FTIR spectrum of PCS reveals shifts of the calcite ν_4 bands from 700 cm^{-1} to 689 cm^{-1} and the peak corresponding to the ν_3 asymmetric stretching vibration of the carbonate group from 1400 cm^{-1} to 1380 cm^{-1} . The carbonyl-related bands of PCS at 1747 and 1644 cm^{-1} , assigned to amide I vibrations, show a noticeable reduction after the kinetic test, indicating that these functional groups may play an active role in Nd(III) immobilization or amorphous neodymium-containing carbonate formation on the sorbent surface. In addition, the band at 874 cm^{-1} , assigned to the ν_2 carbonate vibration, was markedly reduced, and a new band emerged at 841 cm^{-1} , consistent with the carbonate vibration of amorphous dysprosium carbonate reported by Vallina et al. [75]

3.6. Surface morphology and chemical composition of the sorbents

Representative SEM images of the sorbents before and after Nd(III) sorption are presented in Fig. 9, while the corresponding EDS analyses before and after sorption are shown in Supplementary Figs. S21 and S22, respectively. In Fig. 9, panels a-d correspond to PCS, 500, 650, and 800, while labels 1 and 2 indicate the samples before and after sorption, respectively. This section therefore discusses the morphological changes together with the elemental composition of each sorbent.

The PCS sorbent before exposure to the neodymium solution exhibits a dense and relatively smooth morphology with a high calcium content (18 wt%), confirming the dominance of Ca-containing phases. After sorption, the surface becomes rougher and is covered by a continuous secondary precipitate layer. EDS analysis reveals a significant incorporation of Nd (28.2 wt%) along with a drastic reduction in Ca (1.0 wt%), indicating extensive dissolution of Ca-containing phases followed by the formation of Nd-containing phases.

In the case of the 500, the initial morphology shows a heterogeneous structure with moderate Ca content (21.8 wt%). After sorption, the surface is decorated with fine granular and plate-like precipitates. EDS analysis confirms the presence of Nd (23.9 wt%) alongside residual Ca (1 wt%), indicating partial dissolution of Ca-containing phases and subsequent precipitation of Nd-containing compounds.

For the 650, the initial sorbent exhibits a morphology and elemental composition similar to the 500 sample. After sorption, the original surface becomes partially covered with plate-like precipitates. However, EDS analysis shows lower Nd incorporation (7.7 wt%) and higher residual Ca (4.4 wt%) compared with PCS and the 500 sample, suggesting a reduced extent of dissolution of Ca-containing phases and subsequent precipitation.

In contrast, the 800 demonstrates a fundamentally different behavior. The initial sorbent exhibits a less dense, convoluted porous-like structure, reflecting extensive thermal decomposition of carbonate phases. After sorption, relatively large particles with approximately spherical morphology are observed, accompanied by high Nd content (30.1 wt%) and negligible residual Ca. Unlike the other sorbents, a pronounced accumulation of Cl is observed, suggesting the formation of chloride-containing Nd phases or the incorporation of chloride ions during precipitation under highly alkaline conditions. The chlorine may originate from the $NdCl_3$ salt used to prepare the initial Nd(III) solution.

The SEM-EDS results agree well with the sorption behavior and the post-sorption XRD patterns. Higher surface Nd contents were associated with higher Nd(III) removal capacities, whereas the lower Nd content on the 650 sample corresponded to its lower sorption performance. The observed surface precipitates and the crystalline Nd-containing phases detected by XRD further support a removal mechanism based on Ca-phase dissolution followed by Nd-containing phase precipitation.

3.7. Proposed Nd(III) immobilization pathway

As demonstrated by the material characterization results, the four sorbents exhibit distinct removal behaviors governed by their mineralogical composition. In this context, PCS and the 500 and 650 sorbents should be regarded as reactive carbonate-based sacrificial precursors rather than conventional adsorbents. Increasing the pyrolysis temperature reduces surface heterogeneity and induces significant transformations of calcium carbonate phases. Importantly, these carbonate polymorphs including amorphous calcium carbonate, vaterite, and calcite possess markedly different solubility constants [76,77], which can influence the extent of Ca(II) and CO_3^{2-} release into solution.

The XRD results support a carbonate-mediated immobilization pathway for the 500 and 650 sorbents. Neodymium hydroxycarbonate ($NdOHCO_3$) phases were detected after the removal experiments, while the vaterite-related reflections disappeared or were strongly reduced. This indicates preferential dissolution of the more soluble carbonate phase and subsequent formation of Nd-containing precipitates. The FTIR results further support this interpretation, as carbonate vibrations dominated the spectra after reaction and the vaterite-associated band disappeared in the 500 sorbent.

For PCS, no crystalline Nd-bearing phase was detected by XRD after reaction. However, this does not indicate the absence of Nd-containing products. The FTIR spectrum of PCS showed shifts in carbonate-related bands, a marked reduction of the 874 cm^{-1} carbonate band, and the appearance of a new band at 841 cm^{-1} , which is consistent with amorphous neodymium carbonate reported in the literature. The decrease of the carbonyl-related bands at 1747 and 1644 cm^{-1} further suggests that chitin-derived functional groups may have contributed to Nd(III) immobilization or to the stabilization of amorphous Nd-bearing carbonate phases. SEM-EDS also supports this interpretation, showing a secondary precipitate layer, high Nd incorporation, and a strong decrease in Ca after reaction. Thus, the lack of crystalline Nd-bearing reflections in the XRD pattern of PCS is most likely related to poor crystallinity or amorphous product formation rather than the absence of precipitation.

The 800 sorbent followed a different pathway. XRD and FTIR confirmed the presence of highly alkaline CaO and $Ca(OH)_2$ phases in this sorbent material. These phases rapidly increased the solution pH and promoted immediate Nd(III) precipitation as $Nd(OH)_3$. This behavior is consistent with the much larger solubility product of $Ca(OH)_2$ compared with $Nd(OH)_3$ (Ksp $\approx$ 5–8 $\times$ 10^{-6} and 3.2 $\times$ 10^{-22}, respectively), indicating that $Ca(OH)_2$ can dissolve readily while Nd(III) precipitates as $Nd(OH)_3$ under alkaline conditions. [78–80]

As Nd(III) precipitates, OH^- is consumed, which can shift $Ca(OH)_2$ dissolution forward and increase the dissolved Ca(II) concentration. After the rapid precipitation stage, the Ca(II) concentration becomes nearly constant, indicating that the system reached a quasi-steady state controlled by the remaining alkaline Ca-bearing phases. Therefore, the 800 sorbent should be interpreted as a chemically precipitating alkaline material rather than as a conventional sorbent or carbonate-based sacrificial precursor.

4. Conclusion

This study demonstrated that crawfish shell-derived calcium-rich

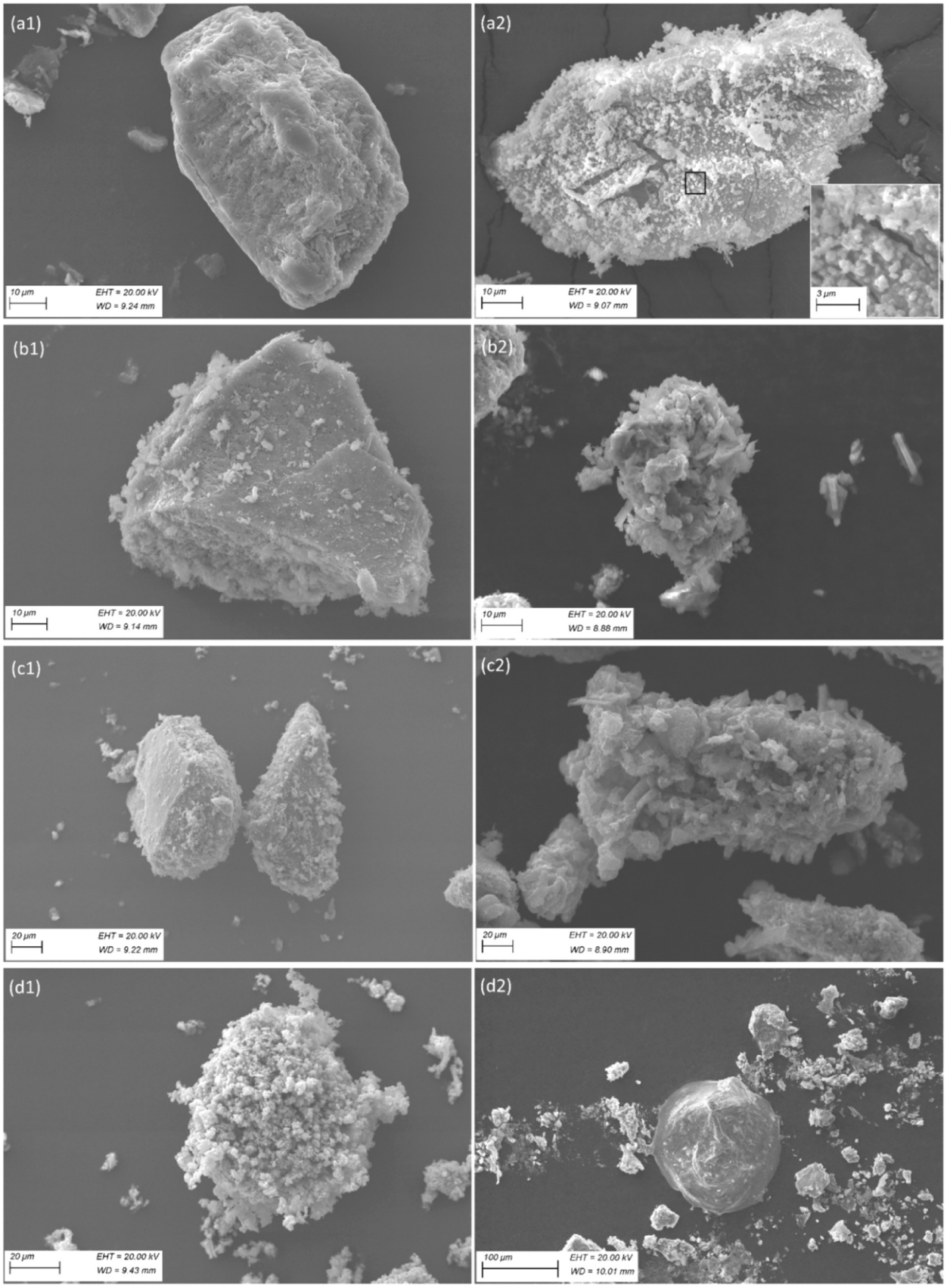

Fig. 9. SEM images of PCS (a), 500 (b), 650 (c), and 800 (d) before (left column) and after the sorption experiment (right column), showing surface morphological changes.

biosorbents can effectively immobilize Nd(III), with performance strongly dependent on sorbent type and sorbent mass. Under the tested conditions, 800 exhibited the highest apparent Nd(III) removal capacity due to instantaneous alkaline precipitation. Among the dissolution-precipitation systems, pristine crawfish shells showed the highest removal capacity, followed by biochars produced at 500 and 650 °C.

The Elovich model provided the best fit to the Nd(III) removal kinetic data, consistent with the heterogeneous nature of the sorbent surfaces and the complexity of the removal process. The strong correlation between Ca(II) release and Nd(III) removal capacity, together with the XRD, FTIR, and SEM-EDS results, indicates that Nd(III) immobilization was primarily governed by a dissolution-precipitation mechanism, with conventional surface adsorption likely playing a secondary role. Pristine crawfish shell likely promoted the formation of an amorphous Nd-containing carbonate phase, whereas the 500 and 650 °C biochars produced crystalline neodymium hydroxycarbonate. Under highly alkaline conditions, 800 °C biochar formed $Nd(OH)_3$.

A novel finding of this study is that dissolution of biogenic calcium carbonate phases and subsequent Nd(III) immobilization occurred at ambient temperature, without the need for thermal treatment. Overall, the process was controlled by the solubility, reactivity, and phase composition of the calcium-bearing substrate. However, the heterogeneous composition of the resulting solids, particularly for pristine crawfish shell, may limit the direct formation of high-purity rare earth products. Future work should therefore focus on post-treatment strategies, such as controlled thermal oxidation and selective separation, as well as selectivity tests in multi-element REE-bearing solutions, to assess the feasibility of this approach for practical rare earth recovery and separation.

CRediT authorship contribution statement

Thomas Elder: Writing – review & editing, Supervision, Investigation, Conceptualization. **Jessica Davis:** Methodology, Data curation. **Yucheng Peng:** Writing – review & editing, Supervision, Resources, Project administration, Funding acquisition, Conceptualization. **Balazs Bencsik:** Writing – original draft, Visualization, Software, Methodology, Investigation, Formal analysis, Data curation, Conceptualization.

Declaration of Competing Interest

The authors declare that they have no known competing financial interests or personal relationships that could have appeared to influence the work reported in this paper.

Acknowledgement

The authors acknowledge financial support from USDA Forest Service [grant no. 24-JV- 11330101–004]; USDA Forest Service Southern Research Station [grant no. 23-JV−11330170–064]. We are grateful to Ruiqi Li, Juan Tarlera Esteves, Haiqiu Jiang and Jonathan Lacuesta Cabral for their assistance in preparing the measurements. We also thank the Soil, Forage, & Water Testing Laboratory at Auburn University for conducting the ICP-OES analyses.

Appendix A. Supporting information

Supplementary data associated with this article can be found in the online version at doi:10.1016/j.jece.2026.123900.

Data Availability

Data will be made available on request.

References

[1] M. Engi, Petrochronology based on REE-minerals: monazite, allanite, xenotime, apatite, Rev. Mineral. Geochem. 83 (1) (2017) 365–418, https://doi.org/10.2138/rmg.2017.83.12.
[2] G. Bailey, et al., Review and new life cycle assessment for rare earth production from bastnäsite, ion adsorption clays and lateritic monazite, Resour. Conserv. Recycl. 155 (2020) 104675, https://doi.org/10.1016/j.resconrec.2019.104675.
[3] A. Gupta, E. Williams, G. Gaustad, Forecasting revenue from primary and secondary sources of rare earth elements, Resour. Conserv. Recycl. 207 (2024) 107612, https://doi.org/10.1016/j.resconrec.2024.107612.
[4] W.L. Leal Filho, R. Kotter, P.G. Özuyar, I.R. Abubakar, J.H.P.P. Eustachio, N. R. Matandirotya, Understanding Rare Earth Elements as Critical Raw Materials, Sustainability 15 (3) (2023) 1919, https://doi.org/10.3390/su15031919.
[5] S.V.S.H. Pathapati, M.L. Free, P.K. Sarswat, A Comparative Study on Recent Developments for Individual Rare Earth Elements Separation, Processes 11 (7) (2023) 2070, https://doi.org/10.3390/pr11072070.
[6] G. Gaustad, E. Williams, A. Leader, Rare earth metals from secondary sources: Review of potential supply from waste and byproducts, Resour. Conserv. Recycl. 167 (2021) 105213, https://doi.org/10.1016/j.resconrec.2020.105213.
[7] D.L. Ramasamy, S. Porada, M. Sillanpää, Marine algae: A promising resource for the selective recovery of scandium and rare earth elements from aqueous systems, Chem. Eng. J. 371 (2019) 759–768, https://doi.org/10.1016/j.cej.2019.04.106.
[8] K. Gallardo, R. Castillo, N. Mancilla, F. Remonsellez, Biosorption of Rare-Earth Elements From Aqueous Solutions Using Walnut Shell, Front. Chem. Eng. 2 (2020) 4, https://doi.org/10.3389/fceng.2020.00004.
[9] M. Butnariu, et al., Remediation of Rare Earth Element Pollutants by Sorption Process Using Organic Natural Sorbents, Int. J. Environ. Res. Public. Health 12 (9) (2015) 11278–11287, https://doi.org/10.3390/ijerph120911278.
[10] R. Rateau, et al., Utilization of Eggshell Waste Calcite as a Sorbent for Rare Earth Element Recovery, ACS Omega 9 (24) (2024) 25986–25995, https://doi.org/10.1021/acsomega.4c00931.
[11] E. Salinas Rodríguez, et al., Ce and Nd Extraction by Cationic Exchange, Using Bentonite, Diatomite, and Eggshell—Preliminary Study, Minerals 13 (6) (2023) 735, https://doi.org/10.3390/min13060735.
[12] K. Vijayaraghavan, R. Balasubramanian, Single and binary biosorption of cerium and europium onto crab shell particles, Chem. Eng. J. 163 (3) (2010) 337–343, https://doi.org/10.1016/j.cej.2010.08.012.
[13] V. Famobuwa, D. Talan, O. Sanyal, S. Grushecky, H. Amini, A review of biomass-based adsorption for rare earth elements recovery, J. Rare Earths 43 (11) (2025) 2311–2321, https://doi.org/10.1016/j.jre.2025.03.006.
[14] E. Fiorito, et al., Calcium carbonate as sorbent for lead removal from wastewaters, Chemosphere 296 (2022) 133897, https://doi.org/10.1016/j.chemosphere.2022.133897.
[15] A.A. Rouff, E.J. Elzinga, R.J. Reeder, N.S. Fisher, The influence of pH on the kinetics, reversibility and mechanisms of Pb(II) sorption at the calcite-water interface, Geochim. Cosmochim. Acta 69 (22) (2005) 5173–5186, https://doi.org/10.1016/j.gca.2005.04.022.
[16] U. Naseer, et al., Fabrication of CaCO3 Microcubes and Mechanistic Study for Efficient Removal of Pb from Aqueous Solution, Materials 17 (22) (2024) 5523, https://doi.org/10.3390/ma17225523.
[17] F. Rees, et al., Metal Immobilization on Wood-Derived Biochars: Distribution and Reactivity of Carbonate Phases, J. Environ. Qual. 46 (4) (2017) 845–854, https://doi.org/10.2134/jeq2017.04.0152.
[18] S.A. Wood, The aqueous geochemistry of the rare-earth elements and yttrium, Chem. Geol. 82 (1990) 159–186, https://doi.org/10.1016/0009-2541(90)90080-Q.
[19] F.J. Millero, Stability constants for the formation of rare earth-inorganic complexes as a function of ionic strength, Geochim. Cosmochim. Acta 56 (8) (1992) 3123–3132, https://doi.org/10.1016/0016-7037(92)90293-R.
[20] J. Schott, O.S. Pokrovsky, E.H. Oelkers, The Link Between Mineral Dissolution/Precipitation Kinetics and Solution Chemistry, Rev. Mineral. Geochem. 70 (1) (2009) 207–258, https://doi.org/10.2138/rmg.2009.70.6.
[21] A.M. Szucs, M. Maddin, D. Brien, P.C. Guyett, J.D. Rodriguez-Blanco, Targeted Crystallization of Rare Earth Carbonate Polymorphs at Hydrothermal Conditions via Mineral Replacement Reactions, Glob. Chall. 7 (2) (2023) 2200085, https://doi.org/10.1002/gch2.202200085.
[22] K. Vijayaraghavan, R. Balasubramanian, Single and binary biosorption of cerium and europium onto crab shell particles, Chem. Eng. J. 163 (3) (2010) 337–343, https://doi.org/10.1016/j.cej.2010.08.012.
[23] J.D. Rodriguez-Blanco, et al., Crystallization, replacement, and redox pathways governing rare earth carbonate and phosphate formation, CrystEngComm 28 (9) (2026) 1453–1469, https://doi.org/10.1039/D5CE01083G.
[24] M. Maddin, et al., Chemical Textures on Rare Earth Carbonates: An Experimental Approach to Mimic the Formation of Bastnäsite, Glob. Chall. 8 (7) (2024) 2400074, https://doi.org/10.1002/gch2.202400074.
[25] A.M. Szucs, A. Stavropoulou, C. O'Donnell, S. Davis, J.D. Rodriguez-Blanco, Reaction Pathways toward the Formation of Bastnäsite: Replacement of Calcite by Rare Earth Carbonates, Cryst. Growth Des. 21 (1) (2021) 512–527, https://doi.org/10.1021/acs.cgd.0c01313.
[26] B. Vallina, J.D. Rodriguez-Blanco, A.P. Brown, J.A. Blanco, L.G. Benning, The role of amorphous precursors in the crystallization of La and Nd carbonates, Nanoscale 7 (28) (2015) 12166–12179, https://doi.org/10.1039/C5NR01497B.
[27] L. Terribili, A.M. Szucs, M. Maddin, K.P. Zubovic, R. Rateau, J.D. Rodriguez-Blanco, Mechanistic Insights into the Early-Stage Crystallization and Nanophase

Formation of Metastable Light Rare-Earth Carbonates, Cryst. Growth Des. 25 (4) (2025) 945–962, https://doi.org/10.1021/acs.cgd.4c01168.
[28] L.C. Hsu, Synthesis and stability of bastnaesites in a part of the system (Ce,La)-F-H-C-O, Mineral. Petrol. 47 (1) (1992) 87–101, https://doi.org/10.1007/BF01165299.
[29] A. Putnis, Mineral replacement reactions: from macroscopic observations to microscopic mechanisms, Mineral. Mag. 66 (5) (2002) 689–708, https://doi.org/10.1180/0026461026650056.
[30] J.M. Astilleros, C.M. Pina, L. Fernández-Díaz, M. Prieto, A. Putnis, Nanoscale phenomena during the growth of solid solutions on calcite {101¯4} surfaces, Chem. Geol. 225 (3–4) (2006) 322–335, https://doi.org/10.1016/j.chemgeo.2005.08.025.
[31] B. Vallina, J.D. Rodriguez-Blanco, A.P. Brown, J.A. Blanco, L.G. Benning, Amorphous dysprosium carbonate: characterization, stability, and crystallization pathways, J. Nanopart. Res. 15 (2) (2013) 1438, https://doi.org/10.1007/s11051-013-1438-3.
[32] M. Zavarin, S.K. Roberts, N. Hakem, A.M. Sawvel, A.B. Kersting, Eu(III), Sm(III), Np(V), Pu(V), and Pu(IV) sorption to calcite, Radiochim. Acta 93 (2) (2005) 93–102, https://doi.org/10.1524/ract.93.2.93.59413.
[33] B. Piriou, M. Fedoroff, J. Jeanjean, L. Bercis, Characterization of the Sorption of Europium(III) on Calcite by Site-Selective and Time-Resolved Luminescence Spectroscopy, J. Colloid Interface Sci. 194 (2) (1997) 440–447, https://doi.org/10.1006/jcis.1997.5115.
[34] K. Sawada, Abdel-Aal, K. Tan, K. Satoh, Adsorption of lanthanoid ions on calcite, Dalton Trans. (20) (2005) 3291, https://doi.org/10.1039/b506688c.
[35] J.-H. Park, J.J. Wang, R. Xiao, B. Zhou, R.D. Delaune, D.-C. Seo, Effect of pyrolysis temperature on phosphate adsorption characteristics and mechanisms of crawfish char, J. Colloid Interface Sci. 525 (2018) 143–151, https://doi.org/10.1016/j.jcis.2018.04.078.
[36] J. Yan, Y. Xue, L. Long, Y. Zeng, X. Hu, Adsorptive removal of As(V) by crawfish shell biochar: batch and column tests, Environ. Sci. Pollut. Res. 25 (34) (2018) 34674–34683, https://doi.org/10.1007/s11356-018-3384-1.
[37] C. Aharoni, F.C. Tompkins, Kinetics of Adsorption and Desorption and the Elovich Equation, in: Advances in Catalysis, 21, Elsevier, 1970, pp. 1–49, https://doi.org/10.1016/S0360-0564(08)60563-5.
[38] J. Wang, X. Guo, Adsorption kinetic models: Physical meanings, applications, and solving methods, J. Hazard. Mater. 390 (2020) 122156, https://doi.org/10.1016/j.jhazmat.2020.122156.
[39] F.-C. Wu, R.-L. Tseng, R.-S. Juang, Characteristics of Elovich equation used for the analysis of adsorption kinetics in dye-chitosan systems, Chem. Eng. J. 150 (2–3) (2009) 366–373, https://doi.org/10.1016/j.cej.2009.01.014.
[40] S. Chen, S. Jiang, H. Jiang, A review on conversion of crayfish-shell derivatives to functional materials and their environmental applications, J. Bioresour. Bioprod. 5 (4) (2020) 238–247, https://doi.org/10.1016/j.jobab.2020.10.002.
[41] P. Romano, H. Fabritius, D. Raabe, The exoskeleton of the lobster Homarus americanus as an example of a smart anisotropic biological material☆, Acta Biomater. 3 (3) (2007) 301–309, https://doi.org/10.1016/j.actbio.2006.10.003.
[42] I. Garcia Alonso, Thermoanalytical studies on lobster shell, J. Therm. Anal. 27 (2) (1983) 257–262, https://doi.org/10.1007/BF01914661.
[43] M. Jang, B. Kong, Y. Jeong, C.H. Lee, J. Nah, Physicochemical characterization of α-chitin, β-chitin, and γ-chitin separated from natural resources, J. Polym. Sci. Part. Polym. Chem. 42 (14) (2004) 3423–3432, https://doi.org/10.1002/pola.20176.
[44] E. Podgorbunskikh, T. Kuskov, D. Rychkov, O. Lomovskii, A. Bychkov, Mechanical Amorphization of Chitosan with Different Molecular Weights, Polymers 14 (20) (2022) 4438, https://doi.org/10.3390/polym14204438.
[45] Y. Wang, et al., Crayfish Carapace Powder Adsorbing Heavy Metal Ions from Aqueous Solution: Capacity, Characterization, Mechanism, J. Aquat. Food Prod. Technol. 25 (1) (2016) 122–130, https://doi.org/10.1080/10498850.2013.830278.
[46] A.W. Ritchie, et al., Reversed crystal growth of rhombohedral calcite in the presence of chitosan and gum arabic, CrystEngComm 15 (47) (2013) 10266, https://doi.org/10.1039/c3ce41543k.
[47] D. Konopacka-Łyskawa, Synthesis Methods and Favorable Conditions for Spherical Vaterite Precipitation: A Review, Crystals 9 (4) (2019) 223, https://doi.org/10.3390/cryst9040223.
[48] F. Manoli, E. Dalas, Spontaneous precipitation of calcium carbonate in the presence of chondroitin sulfate, J. Cryst. Growth 217 (4) (2000) 416–421, https://doi.org/10.1016/S0022-0248(00)00514-5.
[49] S.J. Portugal, J. Bowen, C. Riehl, A rare mineral, vaterite, acts as a shock absorber in the eggshell of a communally nesting bird, Ibis 160 (1) (2018) 173–178, https://doi.org/10.1111/ibi.12527.
[50] Y. Ma, S. Berland, J.-P. Andrieu, Q. Feng, L. Bédouet, What is the difference in organic matrix of aragonite vs. vaterite polymorph in natural shell and pearl? Study of the pearl-forming freshwater bivalve mollusc Hyriopsis cumingii, Mater. Sci. Eng. C. 33 (3) (2013) 1521–1529, https://doi.org/10.1016/j.msec.2012.12.057.
[51] A.L. Soldati, D.E. Jacob, U. Wehrmeister, W. Hofmeister, Structural characterization and chemical composition of aragonite and vaterite in freshwater cultured pearls, Mineral. Mag. 72 (2) (2008) 579–592, https://doi.org/10.1180/minmag.2008.072.2.579.
[52] D.J. Sutor, S.E. Wooley, Gallstone of Unusual Composition: Calcite, Aragonite, and Vaterite, Science 159 (3819) (1968) 1113–1114, https://doi.org/10.1126/science.159.3819.1113.
[53] R. Wei, Z. Peng, J. Wang, Q. Xue, H. Zuo, Waste crayfish shell addition improves mechanical strength and reducibility of hematite briquettes, Biomass Bioenergy 201 (2025) 108107, https://doi.org/10.1016/j.biombioe.2025.108107.
[54] M. Ni, B.D. Ratner, Differentiating calcium carbonate polymorphs by surface analysis techniques—an XPS and TOF-SIMS study, Surf. Interface Anal. 40 (10) (2008) 1356–1361, https://doi.org/10.1002/sia.2904.
[55] N. Vagenas, Quantitative analysis of synthetic calcium carbonate polymorphs using FT-IR spectroscopy, Talanta 59 (4) (2003) 831–836, https://doi.org/10.1016/S0039-9140(02)00638-0.
[56] G. Cárdenas, G. Cabrera, E. Taboada, S.P. Miranda, Chitin characterization by SEM, FTIR, XRD, and^{13} C cross polarization/mass angle spinning NMR, J. Appl. Polym. Sci. 93 (4) (2004) 1876–1885, https://doi.org/10.1002/app.20647.
[57] Y. Egi, J. Kadokawa, Synthesis of Mixed Chitin Esters via Acylation of Chitin in Deep Eutectic Solvents, Molecules 28 (24) (2023) 8132, https://doi.org/10.3390/molecules28248132.
[58] J.-H. Park, J.J. Wang, R. Xiao, B. Zhou, R.D. Delaune, D.-C. Seo, Effect of pyrolysis temperature on phosphate adsorption characteristics and mechanisms of crawfish char, J. Colloid Interface Sci. 525 (2018) 143–151, https://doi.org/10.1016/j.jcis.2018.04.078.
[59] F.S. Kodeh, I.M. El-Nahhal, E.A. Elkhair, A.H. Darwish, Synthesis of CaO–Ag-NPs @CaCO3 Nanocomposite via Impregnation of Aqueous Sol Ag-NPs onto Calcined Calcium Oxalate, Chem. Afr. 3 (3) (2020) 679–686, https://doi.org/10.1007/s42250-019-00112-8.
[60] J. Wang, X. Guo, Adsorption kinetic models: Physical meanings, applications, and solving methods, J. Hazard. Mater. 390 (2020) 122156, https://doi.org/10.1016/j.jhazmat.2020.122156.
[61] S. Demir, et al., Extraction of Lanthanide and Actinide Ions from Aqueous Mixtures Using a Carboxylic Acid-Functionalized Porous Aromatic Framework, ACS Cent. Sci. 2 (4) (2016) 253–265, https://doi.org/10.1021/acscentsci.6b00066.
[62] C. Gok, Neodymium and samarium recovery by magnetic nano-hydroxyapatite, J. Radioanal. Nucl. Chem. 301 (3) (2014) 641–651, https://doi.org/10.1007/s10967-014-3193-z.
[63] D. Saha, S.D. Akkoyunlu, R. Thorpe, D.K. Hensley, J. Chen, Adsorptive recovery of neodymium and dysprosium in phosphorous functionalized nanoporous carbon, J. Environ. Chem. Eng. 5 (5) (2017) 4684–4692, https://doi.org/10.1016/j.jece.2017.09.009.
[64] M.P. Milner, M. Yang, R.G. Compton, Vaterite Dissolution: Mechanism and Kinetics, J. Phys. Chem. C. 128 (25) (2024) 10388–10396, https://doi.org/10.1021/acs.jpcc.4c02074.
[65] R. Sasamoto, Y. Kanda, S. Yamanaka, Difference in cadmium chemisorption on calcite and vaterite porous particles, Chemosphere 297 (2022) 134057, https://doi.org/10.1016/j.chemosphere.2022.134057.
[66] W. Zhu, J. Ma, L. Xu, W. Zhang, Y. Chen, Controlled synthesis of Nd(OH)3 and Nd2O3 nanoparticles by microemulsion method, Mater. Chem. Phys. 122 (2–3) (2010) 362–367, https://doi.org/10.1016/j.matchemphys.2010.03.004.
[67] R. Hay, G. Kashwani, K. Celik, Carbonation, strength development, and characterization of calcined limestone as a potential construction material, Cem. Concr. Res. 139 (2021) 106263, https://doi.org/10.1016/j.cemconres.2020.106263.
[68] C. Li, et al., Reaction mechanism of Ca(OH)2-based carbon storage suitable for the production of building materials, Cem. Concr. Compos. 153 (2024) 105737, https://doi.org/10.1016/j.cemconcomp.2024.105737.
[69] Z. Xu, Y. Zhang, Z. Fang, X. Yin, W. Zhu, Controllable synthesis and optical properties of NdOHCO3 dodecahedral microcrystals, Mater. Res. Bull. 45 (1) (2010) 74–79, https://doi.org/10.1016/j.materresbull.2009.08.014.
[70] W.P. Inskeep, P.R. Bloom, Kinetics of Calcite Precipitation in the Presence of Water-soluble Organic Ligands, Soil. Sci. Soc. Am. J. 50 (5) (1986) 1167–1172, https://doi.org/10.2136/sssaj1986.03615995005000050015x.
[71] F. Lang, M. Kaupenjohann, Effect of dissolved organic matter on the precipitation and mobility of the lead compound chloropyromorphite in solution, Eur. J. Soil. Sci. 54 (1) (2003) 139–148, https://doi.org/10.1046/j.1365-2389.2003.00505.x.
[72] Z. Zou, Z. Du, L. Dai, D. Liu, W. Du, "Crystallization mechanisms and size control of metal-organic frameworks: Insights and applications,", Chem. Eng. J. 480 (2024) 148260 https://doi.org/10.1016/j.cej.2023.148260.
[73] B. Vallina, J.D. Rodriguez-Blanco, J.A. Blanco, L.G. Benning, The effect of heating on the morphology of crystalline neodymium hydroxycarbonate, $NdCO_3$ OH, Mineral. Mag. 78 (6) (2014) 1391–1397, https://doi.org/10.1180/minmag.2014.078.6.05.
[74] D. Zhao, Q. Yang, Z. Han, J. Zhou, S. Xu, F. Sun, Biomolecule-assisted synthesis of rare earth hydroxycarbonates, Solid. State Sci. 10 (1) (2008) 31–39, https://doi.org/10.1016/j.solidstatesciences.2007.08.006.
[75] B. Vallina, J.D. Rodriguez-Blanco, A.P. Brown, J.A. Blanco, L.G. Benning, Amorphous dysprosium carbonate: characterization, stability, and crystallization pathways, J. Nanopart. Res. 15 (2) (2013) 1438, https://doi.org/10.1007/s11051-013-1438-3.
[76] L.N. Plummer, E. Busenberg, The solubilities of calcite, aragonite and vaterite in CO2-H2O solutions between 0 and 90°C, and an evaluation of the aqueous model for the system CaCO3-CO2-H2O, Geochim. Cosmochim. Acta 46 (6) (1982) 1011–1040, https://doi.org/10.1016/0016-7037(82)90056-4.
[77] M.P. Milner, M. Yang, R.G. Compton, Vaterite Dissolution: Mechanism and Kinetics, J. Phys. Chem. C. 128 (25) (2024) 10388–10396, https://doi.org/10.1021/acs.jpcc.4c02074.
[78] I.I. Diakonov, B.R. Tagirov, K.V. Ragnarsdottir, Standard Thermodynamic Properties and Heat Capacity Equations for Rare Earth Element Hydroxides: I. La

$(OH)_3$ (s) and $Nd(OH)_3$ (s). Comparison of Thermochemical and Solubility Data, ract 81 (2) (1998) 107–116, https://doi.org/10.1524/ract.1998.81.2.107.
[79] R.S. Tobias, A.B. Garrett, The Thermodynamic Properties of Neodymium Hydroxide $Nd(OH)_3$, in Acid, Neutral and Alkaline Solutions at 25°; the Hydrolysis of the Neodymium and Praseodymium Ions, Nd^{3+}, Pr^{3+}, J. Am. Chem. Soc. 80 (14) (1958) 3532–3537, https://doi.org/10.1021/ja01547a011.
[80] Chemical Rubber Company, CRC handbook of chemistry and physics: a ready-reference book of chemical and physical data, 86. ed. Boca Raton: CRC Press, 2005.